Electronic structure of matter at high compression: Isostructural transitions and approach of the Fermi-gas limit

J. Meyer-ter-Vehn and W. Zittel*
Max-Planck-Institut für Quantenoptik, D-8046 Garching bei München, Federal Republic of Germany
(Received 16 July 1987; revised manuscript received 11 January 1988)

This paper is concerned with the effect of atomic-shell structure on the cold pressure of highly compressed matter up to 1 Gbar and above. The method is to compare band-structure calculations based on augmented spherical waves with results of the quantum-statistical model. Elements treated explicitly are Li, He, Be, Al, and K. No indication for anomalies due to pressure ionization is found. However, an oscillatory behavior of cold-pressure curves is systematically obtained due to isostructural electronic transitions. They are traced back to pressure-induced band shifts and electron redistribution from bands of low angular momentum (typically s and p waves) to bands of higher angular momentum (typically d and f waves). The shifts are shown to occur generally when squeezing normal matter with extended atoms into highly degenerate matter. The anomalies are particularly pronounced for alkali metals: Strong pressure flattening is found for Li at fivefold compression and 5–10 Mbar, and very sharply for K somewhat below fivefold compression and 500 kbar. The oscillations are much weaker for Be and Al. Metallization of He is obtained at 12.1 g/cm^3 and 110 Mbar. For Be, a structural hcp→bcc transition at 2 Mbar is predicted.

I. INTRODUCTION

High-power laser[1] and particle[2] beams as well as other methods[3] for generating high local energy density offer new possibilities to investigate matter under very high pressure up to 10^8 bars and beyond. For inertial confinement fusion, central pressures up to 10^{12} bars are envisioned by spherical implosion of small spheres; isentropic compression using shaped pressure pulses to keep the material as cold as possible is an important requirement for this purpose.[4] In nature, comparable pressures are found only in the centers of stars and planets; e.g., Jupiter reaches a central pressure of more than 100 Mbar, close to the atomic pressure unit $e^2/a_B^4 \approx 300$ Mbar (e is the electron charge, a_B the Bohr radius). Recent reviews on equations of state (EOS) of matter under high pressure were presented by Bushman and Fortov,[5] by Godwal *et al.*,[6] and by Ross.[7]

The present paper is on the electronic structure of cold matter under high pressure, on how its band structure changes with increasing compression, and how it merges into Fermi-gas behavior asymptotically. Statistical models, the Thomas-Fermi model and its descendants, are believed to hold at pressures above 300 Mbar, but little is known about how the statistical-model limits are approached from below. In this paper, band-structure calculations are compared with the quantum-statistical model for a number of selected elements.

Our major interest is concerned with anomalies of the cold-pressure EOS $p(\rho)$ due to atomic-shell structure (p is the pressure, ρ the matter density). In the literature, results on such anomalies are ambiguous. First-order phase transitions were predicted by Kirzhnits[8] to occur up to very high pressure whenever an inner atomic shell becomes delocalized due to compression. This process of squeezing out bound states into the continuum is called pressure ionization. Large pressure discontinuities in $p(\rho)$ as a consequence of pressure ionization were also reported by Zink,[9] but instead of the pressure flattening predicted by Kirzhnits he obtained pressure steepening. These calculations were criticized by More[10] since they combine a quantum treatment of bound electrons with a statistical description of continuum electrons in an illegitimate way. This method does not account for the quantum effects of level broadening and resonance-state formation near the boundary between the discrete and continuous spectra. These effects form the energy bands in condensed matter and tend to smooth out any sudden transitional behavior. A first step to account for this was done by Lee and Thorsos;[11] their treatment of resonance states changed the pressure jumps of Zink into a much more gradual pressure steepening. But still a steepening due to pressure ionization is in conflict with the pressure flattening postulated by Kirzhnits.

A clarification of these contradictory results can only be obtained from a complete quantum-mechanical band-structure calculation. Pioneering work was done by Voropinov, Gandelman, and Podvalnyi,[12] who calculated cold-compression curves quantum mechanically for elements across the Periodic Table. The drawback of this early work is its limited accuracy due to insufficient treatment of electron exchange and other approximations which were introduced to reduce the numerical complexity. Larger-scale band-structure calculations for the high-pressure EOS of Al were performed more recently by McMahan and Ross,[13] using the augmented-plane-wave method (APW); a comparison of these results with the quantum-statistical model (QSM) was given by More.[14]

In the present paper, the problem is studied more sys-

tematically for a number of materials. Band-structure calculations based on the augmented-spherical-wave (ASW) method[15] are compared with QSM results over a wide range of densities and pressures. The investigation is restricted to zero temperature. The theoretical basis of the QSM and the ASW method is outlined in Secs. II B–II D. For general orientation, Fig. 1 shows empirical Wigner-Seitz cell radii of solids at normal density versus atomic number.[16] At the bottom, the atomic states are given in the order in which they are filled in free atoms. The atomic radii have a maximum for elements with s-state valence electrons and a minimum for the d-state metals in between. Band-structure calculations like the ASW method reproduce the empirical radii almost quantitatively, whereas the statistical model describes solids at normal density only in a very rough and average way. The smooth solid curves show QSM results which differ in the strength σ of the gradient correction (see Sec. II C).

The elements selected for detailed study are marked in Fig. 1 by solid dots. In addition to aluminum as a standard reference case, two alkali metals, lithium and potassium were chosen since they have s-state valence electrons and are found to have anomalous cold-pressure curves. The sequence helium, lithium, beryllium was chosen to study the systematics of the anomaly as a function of Z. These few-electron elements are also convenient for reasons of computational economy. The results are presented in detail in Sec. III, and a concluding discussion is given in Sec. IV.

II. THEORY

A. The degenerate Fermi gas

The pressure of highly compressed, cold matter stems from the kinetic energy of degenerate electrons. Ultimately, for very high compression, it approaches the pressure of the degenerate Fermi gas,

$$p_F=\tfrac{2}{5}\bar{n}E_F\ , \tag{1}$$

where the Fermi energy is given by

$$E_F=(\hbar^2/2m)(3\pi^2\bar{n})^{2/3} \tag{2}$$

or, if necessary, by the corresponding relativistic expression. Here, $\hbar=h/2\pi$ is Planck's constant and m the electron mass. The average electron density

$$\bar{n}=Z\rho/Am_{\mathrm{H}} \tag{3}$$

is obtained from the matter density ρ, the atomic charge Z, and mass number A of the material, and the nuclear mass unit m_{H}.

The electrostatic potential of the ions distorts the ideal

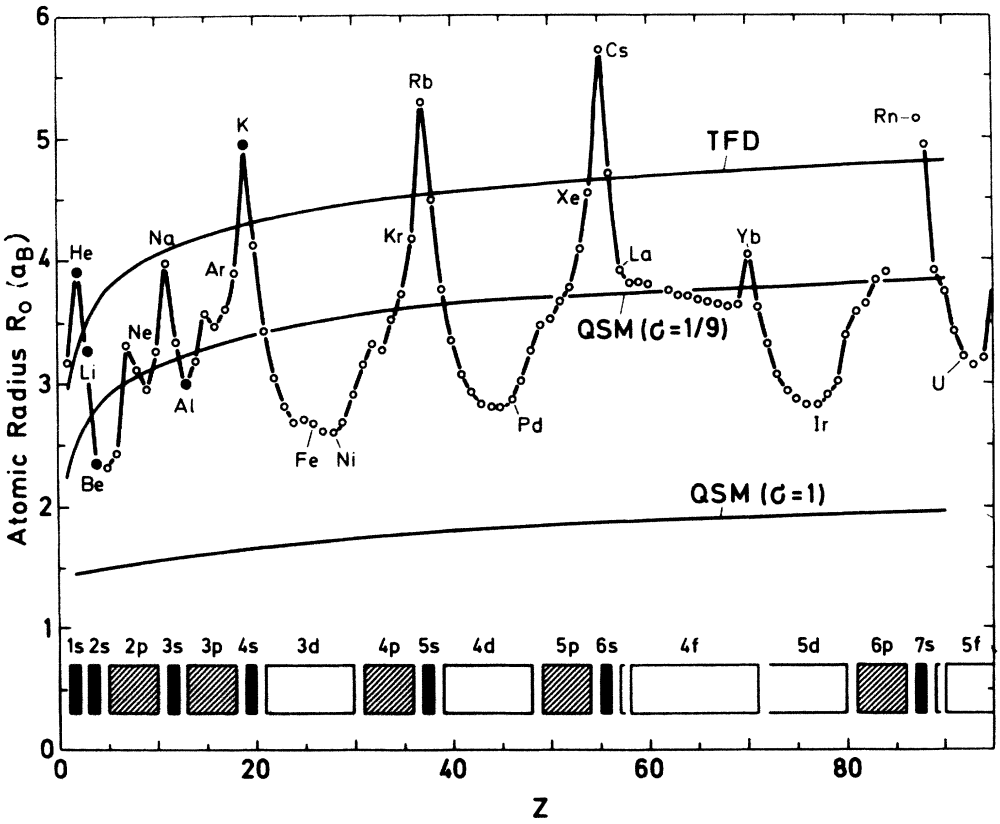

FIG. 1. Atomic Wigner-Seitz radii as a function of atomic number Z. All dots give empirical values taken from Ref. 16; solid dots mark those elements treated explicitly in this paper. The smooth full solid lines give results of the quantum-statistical model (QSM) for different values σ of the gradient correction; TFD corresponds to $\sigma=0$. As the inset at the bottom, electron states are shown in the order in which they are filled in free atoms.

Fermi gas. For the periodic lattice structure of cold matter, is is convenient to consider spherical atomic cells around each ion (Wigner-Seitz cells) with radius

$$r_0=(3Z/4\pi\bar{n})^{1/3} . \tag{4}$$

The overall pressure is then essentially given by the electron kinetic-energy density at the cell boundary. In the EOS calculations below, the electron distribution is determined self-consistently within such spherical cells using different methods. The polyhedral shape of the real elementary cell for a given lattice symmetry is accounted for in the ASW band-structure calculations using the muffin-tin approximation; the results of this calculation are then used to derive proper boundary conditions for a spherical cell calculation.

A key element of our EOS analysis will be an angular-momentum decomposition of the electron distribution in the cell. This is natural for deeply bound orbits which have definite angular momentum, but proves also very useful for characterizing band electrons. The asymptotic l distribution, approached at very high compression, is given by the partial-wave expansion of the uniform Fermi gas,[17]

$$Z=[2/(2\pi)^3]\int d^3k\int d^3r\sum_{l,m}|j_l(kr)Y_{lm}(\Omega_r)|^2 , \tag{5}$$

with spherical Bessel functions $j_l(x)$ and spherical harmonics $Y_{lm}(\Omega)$; the r integration is over the volume of the spherical cell and the k integration over the Fermi sphere with radius $k_F=(3\pi^2\bar{n})^{1/3}$. The partial charges q_l which add up to the total charge $Z=\sum_l q_l$ are obtained from Eq. (5) in the form

$$q_l=[2(2l+1)/\pi]\int_0^{k_Fr_0}dx\,x^2[j_l^2(x)-j_{l-1}(x)j_{l+1}(x)] , \tag{6}$$

where $k_Fr_0=(9\pi Z/4)^{1/3}$ depends only on Z. The dependence of q_l on Z is plotted for the lowest angular momenta in Fig. 2. The l distribution of electrons in atomic cells of actual solids differs considerably from the Fermi-gas distribution; the shape of the Coulomb potential strongly favors states of low angular momentum energetically, particularly s states. When compressing the solid, a redistribution of the electrons from lower to higher l states takes place in order to approach the asymptotic distribution. As we shall show below, it is this process which leads systematically to oscillations in the cold-pressure curve.

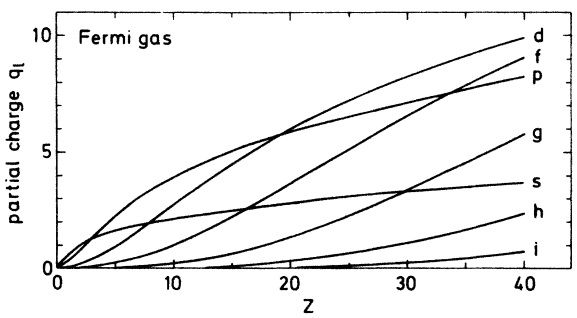

FIG. 2. Partial-wave decomposition of a uniform Fermi gas enclosed in a spherical volume; the partial charges labeled by $s,p,d,$ etc. according to their orbital angular momentum are plotted vs total charge Z.

B. Density-functional description

The compressed matter at zero temperature is modeled like a solid with a fixed, periodic lattice of nuclei and with electrons moving in between. According to Hohenberg and Kohn,[18] the ground-state energy of this many-particle system can be described as the minimum of a density functional

$$E(n)=K(n)+E_{xc}(n)+\int U(\mathbf{r})n(\mathbf{r})d^3r + \frac{e^2}{2}\int\int\frac{n(\mathbf{r})n(\mathbf{r}')}{|\mathbf{r}-\mathbf{r}'|}d^3r\,d^3r' , \tag{7}$$

where $n(\mathbf{r})$ denotes the local electron density. It is obtained from the functional variation

$$\delta E(n)/\delta n=0 \tag{8}$$

under the constraint of electron-number conservation,

$$Z=\int n(\mathbf{r})d^3r . \tag{9}$$

The integrals in Eqs. (7) and (9) extend over the elementary lattice cell with the volume $v=(4\pi/3)r_0^3=Z/\bar{n}$. The hydrostatic pressure is then obtained as the derivative of the total energy with respect to volume,

$$p=-dE/dv . \tag{10}$$

In Eq. (7), a major difficulty is in determining the kinetic energy $K(n)$ and the exchange-correlation energy $E_{xc}(n)$; the potential energy is readily calculated from the electrostatic potential $U(\mathbf{r})$ of the lattice ions and $n(\mathbf{r})$.

Statistical models and quantum-mechanical calculations differ in the way the kinetic energy is treated. In the statistical models, one expands the kinetic energy in terms of derivatives of $n(\mathbf{r})$,

$$K(n)=\int d^3r\,n(\mathbf{r})(\hbar^2/2m) \times[\tfrac{3}{5}(3\pi^2n)^{2/3}+\tfrac{1}{4}\sigma|\nabla n/n|^2+\cdots] . \tag{11}$$

The first term in the square brackets presents the kinetic energy of the free Fermi gas and the second term gives the gradient correction which accounts for nonlocal quantum behavior of the electrons. The strength parameter σ of this term was first derived by Weizsäcker[19] to be $\sigma=1$; however, the systematic expansion[20] of $K(n)$ gives $\sigma=\frac{1}{9}$. This discrepancy was clarified by Jones and Young,[21] who investigated the linear response of a uniform electron gas subject to a small perturbation of wave vector k. They showed that the long-wavelength $[k<k_F=(3\pi^2n)^{1/3}]$ response is reproduced by the Kirzhnits value $\sigma=\frac{1}{9}$ and the short-wavelength $(k\gg k_F)$ response by Weizsäcker's value $\sigma=1$. From this work it appears that $\sigma=\frac{1}{9}$ is the appropriate value to describe integrated atomic properties such as the total energy and the pressure. It will be used in the present work, unless

stated differently. It should be clear that the expression (11) for $K(n)$ represents a rough approximation. It produces continuous, smooth energy spectra and does not account in any way for the discrete spectrum and energy bands which are characteristic of the true quantum mechanics of the electron system. However, this approximation allows for the relative simplicity of the statistical model.

In the quantum-mechanical calculation, the kinetic energy

$$K(n)=\int_{-\infty}^{E_F} dE\, Z(E) \int d^3r\, \psi^*(\mathbf{r},E) \times[(-\hbar^2/2m)\Delta]\psi(\mathbf{r},E) \tag{12}$$

is obtained from the single-electron wave functions $\psi(\mathbf{r},E)$ which also define the local electron density

$$n(\mathbf{r})=\int_{-\infty}^{E_F} dE\, Z(E)\,|\,\psi(\mathbf{r},E)\,|^2 . \tag{13}$$

In zero-temperature matter the energy integration extends over the low-lying states up to the Fermi energy E_F, and $Z(E)$ is the spectral density of states. The calculation of $\psi(\mathbf{r},E)$ within the ASW method will be described below.

For the exchange-correlation energy $E_{xc}(n)$, a local approximation is chosen. The functional derivative

$$V_{xc}=\delta E_{xc}(n)/\delta n = V_{ex}+V_c \tag{14}$$

is expressed by two parts, the exchange potential[22]

$$V_{ex}=-(e^2/\pi)(3\pi^2 n)^{1/3} \tag{15}$$

and the von Barth–Hedin[23] expression for the correlation potential,

$$V_c=-0.022(e^2/a_B)\ln(1+1/x) , \tag{16}$$

with $x=21a_B(4\pi n/3)^{1/3}$ and $a_B=\hbar^2/me^2$.

C. The quantum-statistical model

The equations of the quantum-statistical model are obtained from Eqs. (7)–(9) and (11) in the form

$$(\hbar^2/2m)(3\pi^2 n)^{2/3}+\tfrac{1}{4}\sigma(\,|\,\nabla n/n\,|^2-2\,\Delta n/n) + V_{xc}+V=E_F , \tag{17}$$

with the electrostatic potential

$$V(\mathbf{r})=-\frac{Ze^2}{r}+e^2\int\frac{n(\mathbf{r}')}{|\,\mathbf{r}-\mathbf{r}'\,|}d^3r' . \tag{18}$$

The various versions of the statistical model are contained in these equations. The original Thomas-Fermi (TF) model[24] is recovered when dropping the gradient and the exchange-correlation terms in Eq. (17). Keeping the exchange part (15) of V_{xc} leads to the Thomas-Fermi-Dirac (TFD) model,[25] and including also perturbatively the gradient correction gives the Thomas-Fermi-Kirzhnits model (TFK).[26]

The quantum-statistical model which is used in the present work was first applied to high-pressure EOS calculations by Kalitkin and Kuzmina.[27] A very clear discussion of QSM and its merits for high-density matter calculations was given by More;[14] finite-temperature QSM calculations were reported by Perrot.[28] The QSM is used to solve Eqs. (17) and (18) self-consistently for the atomic cell with all terms included and with the boundary conditions

$$dV/dr=0 \quad \text{and} \quad dn/dr=0 \quad \text{at } r=r_0 , \tag{19a}$$

$$rV(r)\to -Ze^2 \quad \text{for } r\to 0 , \tag{19b}$$

$$dn/dr=-2Zn/\sigma a_B \quad \text{at } r=r_0 , \tag{19c}$$

with $a_B=\hbar^2/me^2$. Treating the gradient term self-consistently may look arbitrary at this point, since it is the first-order term in an expansion and the higher-order terms are neglected; also, this treatment considerably complicates the numerical solution, because it leads essentially to a fourth-order differential equation for $n(r)$. On the other hand, the self-consistent treatment removes the divergence of $n(r)$ for $r\to 0$ which is a deficiency of the other Thomas-Fermi–type models mentioned; the finite density of the QSM at the origin is expressed by boundary condition (19c). It also improves the asymptotic pressure behavior. The pressure is given by

$$p=\tfrac{2}{5}(\hbar^2/2m)(3\pi^2 n_0)^{2/3}n_0-(e^2/4\pi)(3\pi^2 n_0)^{1/3}n_0 + p_c-\tfrac{1}{2}\sigma(\hbar^2/2m)(\Delta n)_0 , \tag{20}$$

where n_0 is the density evaluated at the cell boundary r_0, and p_c is the correlation contribution

$$p_c=0.022(e^2/a_B)n_0[x^3\ln(1+1/x)+x/2-x^2-\tfrac{1}{3}] . \tag{20a}$$

As pointed out by More,[14] the high-density expansion of the pressure (20),

$$p=23.27\bar{n}^{5/3}-(5.68+11.16Z^{2/3})\bar{n}^{4/3}+\cdots , \tag{21}$$

(p in Mbar and the average density $\bar{n}$ in electrons/Å^3), does not depend on σ up to order $\bar{n}^{4/3}$. This is a consequence of the self-consistent treatment and is in agreement with electron-gas perturbation theory which is applicable in the high-density range.

Some points concerning the numerical solution of the QSM equations are discussed in Appendix A.

D. The quantum-mechanical ASW calculation

The main results of this paper are obtained from quantum-mechanical calculations using the augmented-spherical-wave method. These are *ab initio* self-consistent-field (SCF) band-structure calculations. The ASW method was developed by Williams, Kübler, and Gelatt and is described in full detail in Ref. 15; we have used the computer code written by these authors. In the following we give only a brief outline of the basic concept and emphasize a few points specific for applications of the ASW method to highly compressed matter and relevant for the results presented in Sec. III.

The basis for the quantum-mechanical calculation is

the Schrödinger equation for the single-electron wave function,

$$[-(\hbar^2/2m)\Delta+V(\mathbf{r})-E]\psi(\mathbf{r},E)=0\ , \tag{22}$$

which is obtained from functional variation using Eqs. (7)–(9), (12), and (13). The self-consistent potential

$$V(\mathbf{r})=-\sum_{\nu}\frac{Ze^2}{|\mathbf{r}-\mathbf{R}_\nu|}+e^2\int\frac{n(\mathbf{r}')}{|\mathbf{r}-\mathbf{r}'|}d^3r'+V_{\rm xc}(n) \tag{23}$$

consists of the electrostatic potential of the lattice with atomic nuclei of charge Z at the lattice points R_ν, the potential of the electrons, and the exchange-correlation potential $V_{\rm xc}$. Solving Eq. (22), the electron states are divided into core states, which are fully localized at a lattice point and do not contribute to the hydrostatic pressure, and band states, the wave functions of which extend over the whole lattice and generate the pressure. In metals at normal density only a few valence electrons occupy the band states. However, at pressures of 100 Mbar and beyond also core states start to delocalize and to form energy bands. Whereas the core states are completely determined inside an atomic cell, the band states communicate with the neighboring cells through boundary conditions defined at the cell interfaces.

In the ASW method, the band-state wave functions are expanded in a set of spherical waves,

$$\psi(\mathbf{r},E)=\sum_{L,\nu}c_{L\nu}(E)H_L(\mathbf{r}-\mathbf{R}_\nu)\ , \tag{24}$$

where $L=(l,m)$ is a collective index denoting angular-momentum quantum numbers with respect to a cell center and where ν runs over all lattice cells. Each cell is then divided into a central spherical part in which $V(r)$ is assumed to be spherically symmetric and an outer part with a polyhedral surface in which $V(r)=V_0$ is assumed to be constant (muffin-tin approximation). The radial parts of the spherical waves, $H_L(r)$, are then represented in the outer region by Hankel or von Neumann functions depending on whether the "kinetic energy" $\varepsilon=E-V_0$ is negative or positive, respectively. In the inner region, the spherical waves $H_L(r)$ are "augmented" by explicitly integrating the Schrödinger equation. The interstitial energy ε is used as a variational parameter; this is further discussed in Appendix B.

The band-structure part of the ASW calculation determines the expansion coefficients $c_L(E)$ and, from these, the energy-level density

$$Z(E)=\sum_l Z_l(E) \tag{25}$$

decomposed into contributions $Z_l(E)$ of the different partial waves. This is a major part of the calculation, and the reader is referred to Ref. 15 for details. A specific feature of the ASW method is that the density distribution of the band electrons within an atomic cell is not calculated from $\psi(r,E)$ directly, but is determined by

$$n_{\rm band}=\sum_l\int_{-\infty}^{E_F}dE\,Z_l(E)[R_l(r,E)]^2\ , \tag{26}$$

where $R_l(r,E)$ is the radial solution of the Schrödinger equation (22) with angular momentum l and energy E; it is calculated for a spherical atomic cell extended outwards up to the Wigner-Seitz radius r_0 (4). It turns out that $R_l(r,E)$ is almost linear in E across an energy band;[29] therefore, it is possible to further simplify Eq. (26). Representing the first four moments of each $Z_l(E)$,

$$\int_{-\infty}^{E_F}dE\,Z_l(E)E^n=q_{l1}E_{l1}^n+q_{l2}E_{l2}^n\quad(n=0,1,2,3)\ , \tag{27}$$

by two energies E_{l1},E_{l2} and two charges q_{l1},q_{l2}, one obtains

$$n_{\rm band}(r)=\sum_l[q_{l1}R_l^2(r,E_{l1})+q_{l2}R_l^2(r,E_{l2})]\ . \tag{28}$$

The fraction of charge in partial wave l is $q_l=q_{l1}+q_{l2}$, and the number of band electrons is

$$q_{\rm band}=\sum_l q_l\ . \tag{29}$$

The total electron-density distribution in the atomic cell is

$$n(r)=n_{\rm core}(r)+n_{\rm band}(r)\ , \tag{30}$$

with the core density

$$n_{\rm core}(r)=\sum_{n,l}2(2l+1)R_{nl}^2(r)\ , \tag{31}$$

where the sum runs over all core orbits (n,l); the density (30) is then used to redetermine the potential $V(r)$.

The ASW calculation consists of two self-consistency loops. In the inneratomic loop $n(r)$ and $V(r)$ are iterated within the spherical atomic cell for given band-level densities $Z_l(E)$. After convergence, the muffin-tin band-structure calculation is repeated with the new $n(r)$ and $V(r)$ to obtain new $Z_l(E)$. The interface between the interatomic band-structure calculation and the inneratomic loop is established by the set of four numbers $(q_{l1},q_{l2},E_{l1},E_{l2})$ for each l representing $Z_l(E)$. The procedure is iterated until full self-consistency is obtained. A typical time on a Cray-1 computer to achieve full convergence for Al was about 1 min of CPU (central-processing-unit) time.

Finally, the total pressure is also obtained as a sum $p=\sum_l p_l$ of partial-wave contributions,[17]

$$p_l=(1/4\pi^2)\sum_{l,i}q_{li}R_l^2(r_0,E_{li})\left[\frac{D_{li}(D_{li}+1)-l(l+1)}{r_0^2}-V_{\rm eff}(r_0)+E_{li}+V_{\rm xc}(r_0)-E_{\rm xc}(r_0)\right]\ , \tag{32}$$

where D_{li} are logarithmic derivatives $D_{li} = d[\ln R_l(r,E_{li})]/dr$ at the cell boundary $r = r_0$, $V_{\text{eff}}(r_0)$ represents the Hartree contributions to the electrostatic potential, and $V_{\text{xc}}(r_0)$ and $E_{\text{xc}}(r_0)$ are the exchange-correlation contributions defined in Eqs. (7) and (14).

III. RESULTS

A. Overview of calculated materials

An overview of the calculated results is given in Fig. 3. All the materials shown are explicitly investigated in this paper, except for cesium, which has been added for comparison. The quantity plotted is the bulk modulus versus specific volume $v = 1/\rho$,

$$B = -v\, dp/dv \ ,$$

calculated from the pressure curves $p(v)$ at zero temperature within the ASW method. The open circles for $v/v_0 = 1$ give the empirical bulk moduli at normal solid-state volume v_0. The focus of the present work is on the behavior at high compression ratios where the details of lattice structure become of minor importance compared with isostructural transitions. It is this high-compression regime where the effects of pressure ionization might show up and where the approach to statistical-model predictions should occur.

The low compressibility of the alkali metals Li, K, and Cs is related to the large atomic radii R_0 of these elements at normal density, which, in turn, are due to their s-state valence electrons (compare Fig. 1). Isostructural transitions caused by the pressure-induced shift of the s electrons into other valence bands are most pronounced for these elements. In Fig. 3 they show up as large anomalies in the bulk moduli of Cs and K at $v/v_0 = 0.4$ and 0.2, respectively. For Li, the corresponding transition occurs in about the same compression region; however, the anomaly of the bulk modulus is much less pronounced in this case and appears as a series of weak oscillations. These results will be analyzed in detail below.

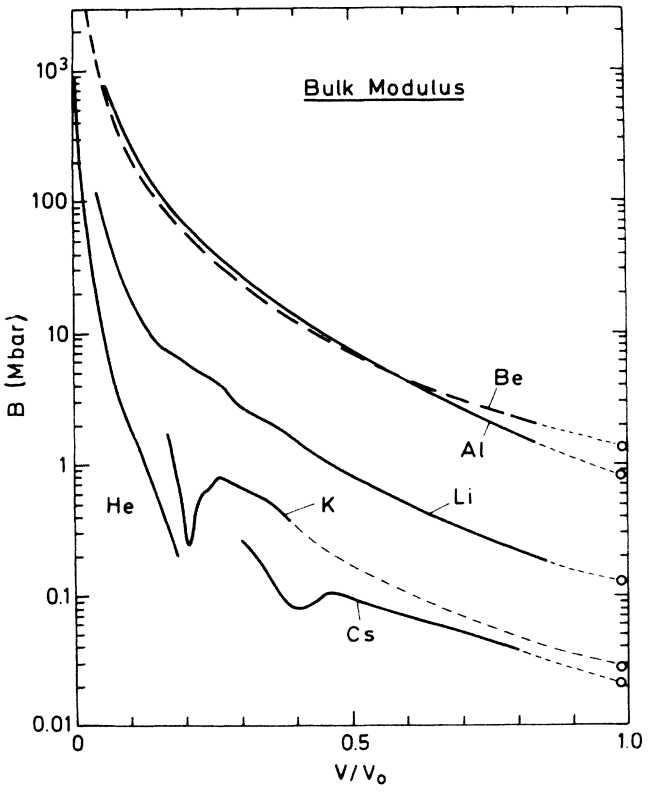

FIG. 3. Calculated bulk modulus B vs specific volume V in units of the zero-pressure volume V_0 for elements investigated in the present paper; only the results for Cs are from Ref. 48.

In order to study these effects more systematically as a function of atomic number, we included helium and beryllium, the elements neighboring lithium, in the present investigation. These light elements were chosen for computational convenience, since the computer time needed quickly rises with the number of electrons. Helium is known as quantum liquid at low temperature; quantum effects inhibit solidification and are responsible for the large atomic volume v_0. However, it solidifies at higher pressure and, at the very high compression considered here, the description in terms of a frozen lattice may be adequate. The metallization of helium will be of particular interest in the following.

The calculated bulk moduli of beryllium and aluminum are very close to each other and considerably larger. They vary smoothly with compression and show no apparent wiggles, at least when plotted logarithmically as in Fig. 3. Careful analysis in the following will uncover some weak oscillations which are also caused by band crossings. However, several valence electrons distributed over different bands contribute to the pressure in these cases and, therefore, no sharp transitional behavior is observed.

In what follows, results for the different materials are discussed in the following order: Li, He, Be, Al, K. Some of these results were already published at other places.

B. Lithium

The cold pressure of lithium[30] as a function of compression is shown in Fig. 4. The ASW band-structure calculation (thick solid line) is compared with two versions of the statistical theory: the Thomas-Fermi model and the quantum-statistical model. Two important features should be noticed: the pronounced flattening of the ASW pressure curve in the range $3 < p < 10$ Mbar and the almost complete agreement between ASW and QSM results for $p > 30$ Mbar.

Two QSM branches are seen at lower pressure; they show the difference between the use of the exchange-correlation potential V_{ex} of Eq. (15) alone and the full use of V_{xc} including the von Barth–Hedin potential V_c [compare Eqs. (14) and (16)], which leads to somewhat lower pressures. A similar difference is obtained in the band calculations when changing from V_{ex} to V_{xc}. The ASW results plotted are obtained with V_{xc} for a bcc lattice. Also shown are recent results of linear combination of Gaussian-type orbitals band calculations of Boettger and Trickey[31] using fcc symmetry and the results of Liber-

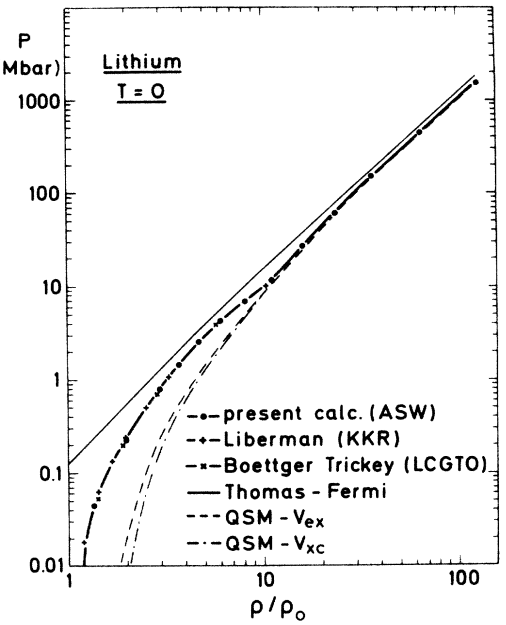

FIG. 4. Calculated cold pressure vs compression for lithium; solid dots represent present ASW calculations; ×, from Ref. 30; +, from Ref. 31; Thomas-Fermi results are given by thin solid line, QSM with V_{ex} dashed, and QSM with V_{xc} dashed-dotted line. Here and in the following plots the compression ρ/ρ_0 is defined as the density ratio with respect to the calculated zero-pressure density ρ_0.

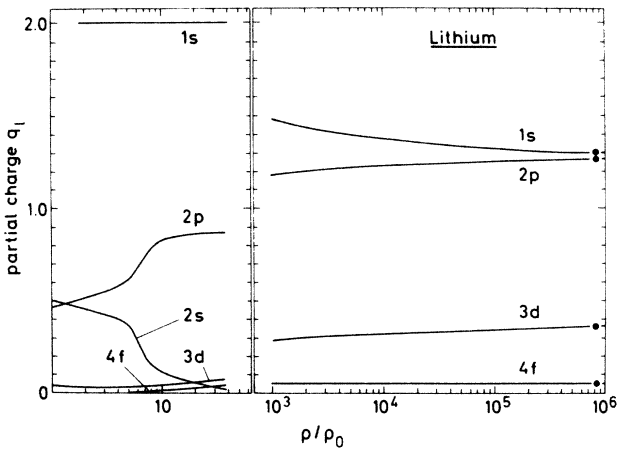

FIG. 5. Partial-wave decomposition of the total charge of lithium vs compression. The ASW results (solid lines) approach the limiting Fermi-gas values indicated as dots on the right-hand side. Results for 100- to 1000-fold compression are omitted for reasons given in the text.

man[32] for Li pressures up to 10 Mbar. Excellent agreement with the present calculations is found, indicating that the high-pressure results are rather insensitive to details of the different methods used and, in particular, to the lattice symmetry chosen. The most stable phase obtained in the ASW calculation is fcc at low pressures and changes to bcc at about 4 Mbar. It is important to note, however, that the difference between the phases is small and that the dominant feature in the cold pressure is of different nature.

The origin of the pressure flattening is investigated in Fig. 5 in terms of the occupation numbers q_l of the different electron orbits l. In normal-density Li, two electrons occupy the $1s$ state and the third electron is shared almost equally by the $2s$ and $2p$ states. Compression then gradually depopulates the $2s$ band in favor of the $2p$ band. At $\rho/\rho_0=6-7$, the reordering accelerates and, at $\rho/\rho_0>10$, the valence electron has predominantly p-wave character. The pressure is sensitive to this $2s\rightarrow 2p$ shift since a $2s$ electron generates considerably more pressure than a $2p$ electron. This is due to the larger radial extension of the $2s$ state. In the present case, an electron in the $2s$ state produces almost 3 times as much pressure as an electron in the $2p$ state. This explains the pressure flattening observed in Fig. 4.

The present lithium calculation was extended to extremely high compression ratios to further investigate possible effects of pressure ionization and the approach to the Fermi-gas limit. The $1s$ core state which is deeply bound at normal density is gradually shifted upwards in energy and broadened with increasing density. The actual delocalization of the $1s$ core electrons may be inferred from Fig. 6, where radial density profiles calculated for different values ρ/ρ_0 are plotted. The maximum of these profiles at small radius indicating a localized $1s$ state disappears at $\rho/\rho_0=37$. This roughly sets the density region in which the pressure ionization of the core occurs. No anomaly of the $p(\rho)$ curve is observed in this region. On the contrary, the pressure curve shown in Fig. 4 evolves smoothly, in close agreement with the QSM predictions at these pressures.

The approach of the Fermi-gas limit at extremely high densities is demonstrated in Figs. 5 and 7. On the right-hand side of Fig. 5, it is shown how the charge distribution over different partial waves evolves at compression ratios up to 10^6. This is to illustrate that the present

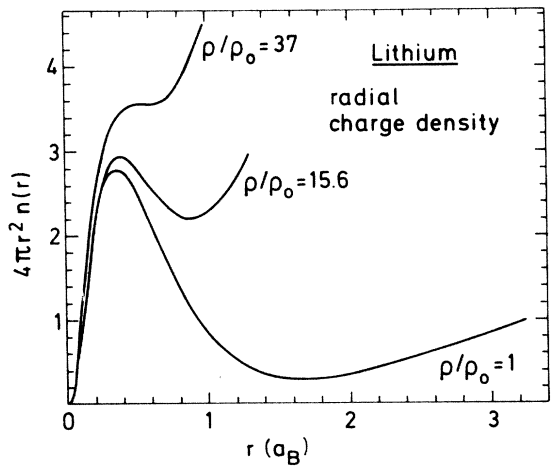

FIG. 6. Radial distribution of the Li electron density for the normal metal and at 15.6- and 37-fold compression. Units of the ordinate are inverse Bohr radii, $1/a_B$.

ASW calculation actually reproduces the angular-momentum distribution of the Fermi gas which was derived in Sec. II A. The Fermi-gas values are given as solid dots on the right-hand side of Fig. 5 and show perfect agreement with the ASW results. A difficulty in producing Fig. 5 with the present version of the ASW code is that the band-structure part does not allow for hybridization of states with the same angular momentum, such as the $1s$ and $2s$ states. Therefore, the region of strong $1s$-$2s$ interaction occurring at 100- to 1000-fold compression for lithium is not properly calculated and has been omitted in Fig. 5. Beyond 1000-fold compression, the $2s$ state is pushed to energies high above the Fermi energy and is replaced by $1s$ as the valence state in the band-structure calculation.

Details of the band calculation at high compression are given in Fig. 7. It shows the energy spectrum along selected symmetry lines of the bcc Brillouin zone for three densities. The dashed horizontal line marks the Fermi energy. At normal density, the band spectrum close to the Fermi surface shows free-electron behavior characterized by the parabolic shape around the Γ point; the deeply bound $1s$ state is not shown in Fig. 7(a). In Fig. 7(b) at 15.6-fold compression, the picture has changed considerably, the $2s$ level at Γ has crossed the Fermi surface, showing an inversion of its curvature which is typical for the $s \rightarrow p$ shift, and the $1s$ state represented by the lowest line is seen to broaden. Figure 7(c) displays the spectrum at 4600-fold compression, which now exhibits almost pure free-electron behavior, expected for the Fermi-gas limit.

C. Helium

Helium is included in the present analysis mainly for illustrative purposes. Certainly, the frozen-lattice approximation used here is not adequate to describe helium at low densities. On the other hand, this simple two-electron system shows some qualitative features which are relevant concerning pressure ionization and the question of how the statistical-model limit is approached.

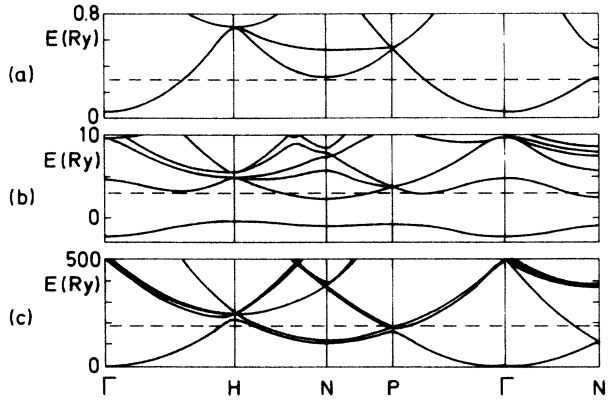

FIG. 7. Lithium electron-energy spectrum in k space along selected symmetry lines of the bcc Brillouin zone; Γ, H, N, and P are the symmetry points. (a) Normal density, (b) 15.6-fold and (c) 4600-fold compression.

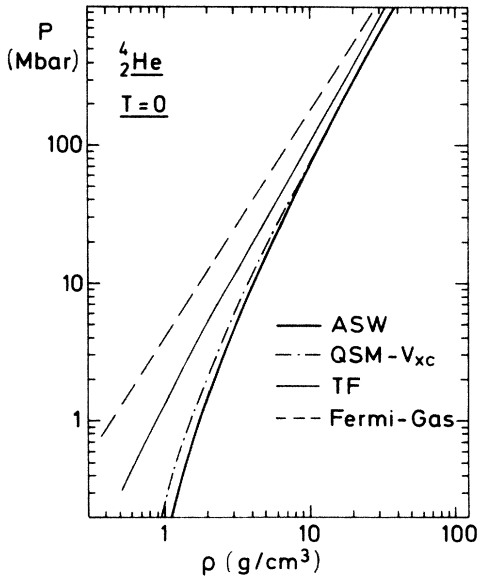

FIG. 8. Cold pressure of helium vs density; ASW results (thick solid line) are compared with QSM (dashed-dotted), Thomas-Fermi (thin solid), and Fermi-gas (dashed) results.

Also, helium serves as an example for metallization at high pressure. A hcp lattice[33] is assumed; however, fcc structure calculations also performed give almost identical results.

The calculated ASW cold-pressure curve $p(\rho)$ is shown in Fig. 8 together with the different statistical-model predictions. The pressure curve $p(\rho)$ is completely smooth and shows no anomaly at densities between 1 and 10 g/cm^3, where pressure ionization of the $1s$ state is found. The results of the band calculation and of the quantum-statistical model merge with each other just at the point of metallization where the upper edge of the filled $1s$ band hits the lower edge of the empty $2p$ band. The $1s$ and $2p$ energy bands versus density are shown in Fig. 9; the band edges have been calculated using Wigner-Seitz boundary

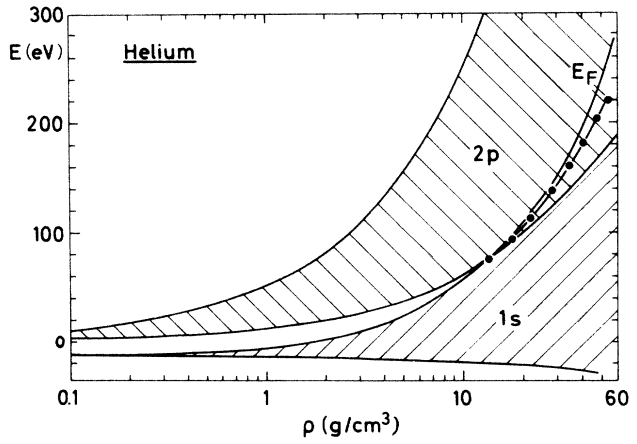

FIG. 9. Helium energy bands vs density. Metallization sets in at a density of 12 g/cm^3 when the filled $1s$ band starts to overlap with the unfilled $2p$ band; solid dots mark the Fermi energy E_F.

conditions. The metallization pressure of 110 Mbar calculated here is in good agreement with the result of Young *et al.*,[34] who obtained 112 Mbar. Also, the metallization density of 12.1 g/cm^3 corresponding to a Wigner-Seitz radius of $0.915a_B$ compares well with the value $0.91a_B$ quoted by March.[35]

D. Beryllium

Beryllium is the other neighboring element of lithium with atomic number $Z=4$. It was chosen to investigate how the anomaly observed in lithium changes when having two valence electrons instead of one. Since information on the high-pressure phases of Be is lacking in the literature, we also include some ASW results on phase stability.

The cold-pressure curve is shown in Fig. 10, again in comparison with the corresponding TF and QSM results. The band calculation describes the tighter binding of beryllium which leads to a normal solid density larger than the QSM value. The ratio between the calculated and the empirical solid-state density is 1.14. There is good agreement for the pressures at higher density between earlier linear muffin-tin orbital calculations[36] and the present ASW results.

The partial charges in the different bands are given in Fig. 11 and should be compared with the results for lithium in Fig. 5. The second valence electron of Be is added almost exclusively to the $2p$ state, and the $2s$ state and its depopulation with increasing density is therefore of less importance for the cold-pressure curve. Its flattening due to $2s \rightarrow 2p$ reordering, which shows up so sharply for Li in Fig. 4, is also visible for Be in Fig. 10 in the range of 10- to 50-fold compression, but in considerably weaker form.

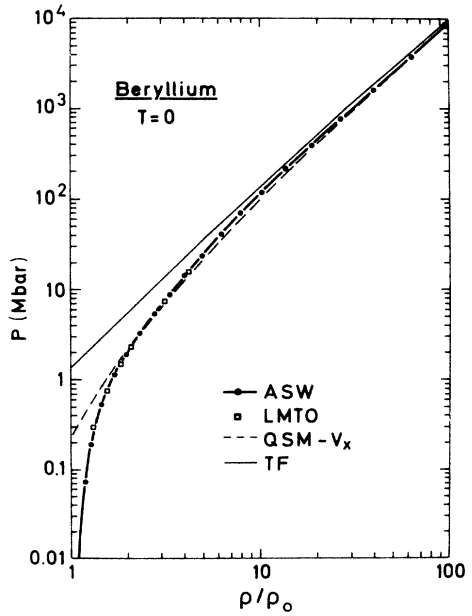

FIG. 10. Cold pressure of beryllium vs compression; solid dots represent ASW results, open squares earlier LMTO results from Ref. 36, thin solid line Thomas-Fermi, and dashed line QSM results.

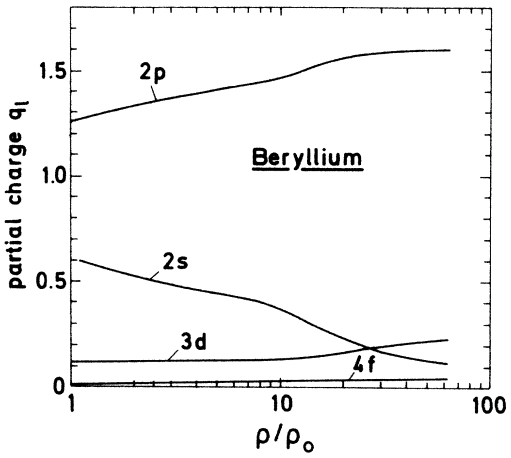

FIG. 11. Partial-wave decomposition of Be valence charge; compare Fig. 5.

We emphasize that pressure ionization of the $1s$ state which sets in at about $\rho/\rho_0=20$ does not contribute to the pressure anomaly. The calculated $1s$ contribution to the total pressure develops in a completely smooth manner.

Complete merging of ASW and QSM pressures occurs at 50-fold compression. This is just the region where the gap between the broadened $1s$ core state and the $2p$ band closes. At this density, the distribution of the four Be electrons, listed in Table I for different densities, is still far from the limiting Fermi-gas distribution. It appears that the final reordering is described within the quantum-statistical model and occurs in a smooth fashion.

We add here some structural results obtained in the present ASW calculation. The stable phase of Be at normal density was determined by Chou *et al.*[37] to be hcp with a ratio of the lattice constants $c/a=1.586$. In Table II, ASW binding energies for bcc, fcc, and hcp symmetry are given as a function of the Wigner-Seitz radius. It is seen that the stability changes from hcp to bcc at $r_0 \approx 2a_B$, corresponding to a density of 2.7 g/cm^3 and a pressure of about 3 Mbar. At normal density, we find $c/a=1.56$ as the optimal ASW value that should be compared with the experimental value[38] $c/a=1.57$.

E. Aluminum

Aluminum with ten electrons in the $1s$, $2s$, and $2p$ core states and three valence electrons in the $3s$, $3p$, and $3d$

TABLE I. Partial charges of Be at different densities.

Partial wave	s	p	d	f
Free atom ($\rho=0$)	4	0	0	0
Solid ($\rho=\rho_0$)	2.61	1.26	0.12	0.01
Compressed solid ($\rho=50\rho_0$)	2.13	1.60	0.23	0.04
Fermi-gas limit ($\rho\rightarrow\infty$)	1.49	1.76	0.63	0.11

TABLE II. Be binding energies in Ry.

r_0/a_B	bcc	fcc ($c/a=1.633$)	hcp
2.30	29.2289	29.2290	29.2345
2.25	29.2265	29.2266	29.2306
2.20	29.2239	29.2239	29.2277
2.10	29.2105	29.2103	29.2135
2.00	29.1841	29.1834	29.1859
1.90	29.1382	29.1370	29.0653
1.80	29.0667	29.0650	
1.60	28.8070	28.8034	
1.40	28.2769	28.2703	

states is more complex than the elements considered so far. The high-pressure phases of Al were studied recently by Lam and Cohen,[39] indicating a fcc→hcp transition at 2 Mbar and a hcp→bcc transition at 4 Mbar. In the present ASW calculation, a fcc lattice is assumed, as was done in the APW calculations for compressed Al by McMahan and Ross.[13] The cold-pressure results are shown in Fig. 12 and the corresponding band plot in Fig. 13. It is seen that both the $3s$ and $3p$ bands are strongly pushed upwards with increasing compression, driven by the $2s$ and $2p$ core states of same symmetry, whereas the $3d$ band, having no core state of the same symmetry, is relatively lowered.

The electron reordering upon compression, shown in Fig. 14, occurs, therefore, predominantly from $3s$ and $3p$ to $3d$, and also to $4f$ at higher densities. At very high density beyond 1000-fold compression, even the $2s$ state starts to be emptied in favor of the $3d$ and $4f$ states. Again it is interesting to compare this with the partial charges which have to be reached ultimately in the Fermi-gas limit and are given in Table III. Even at 1000-fold compression one is still far from this limit.

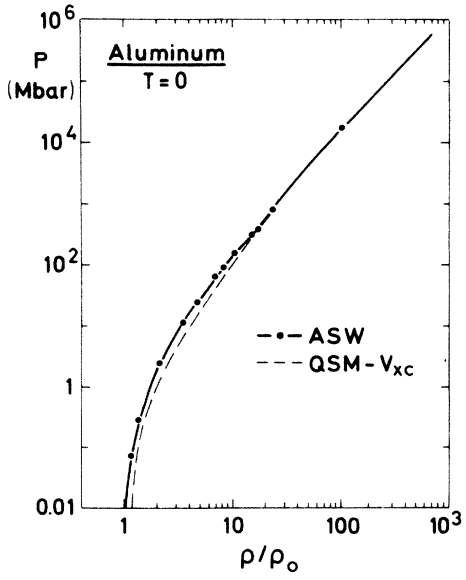

FIG. 12. Cold pressure of aluminum vs compression; ASW results are given by solid dots, QSM results by dashed line.

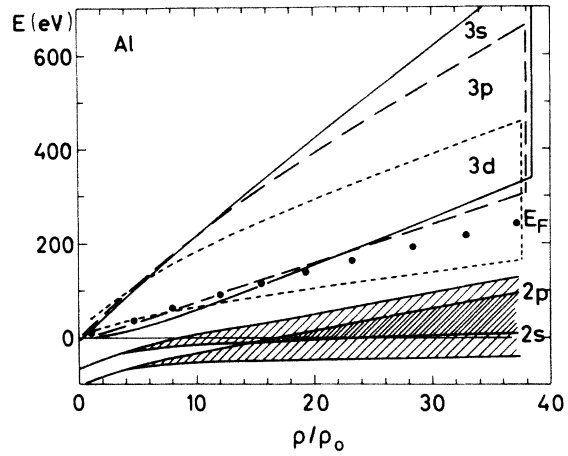

FIG. 13. Aluminum energy bands vs compression.

The pressure anomaly caused by the $3s,3p \rightarrow 3d$ band reordering occurs at tenfold compression. It is clearly seen in Fig. 12. From the present calculation we can exclude that the anomaly originates from pressure ionization, as was claimed in Ref. 13. Though it is true that pressure ionization of the L shell also occurs around tenfold compression, the behavior of the $2s$ and $2p$ pressure contributions is completely smooth in this region. Also, the second, much weaker pressure flattening, which McMahan and Ross found at about 1000-fold compression and which they attributed to K-shell pressure ionization, finds its natural explanation in Fig. 14 as a $2s \rightarrow 3d,4f$ electron redistribution. We have checked that the partial pressure of the K shell shows no anomaly in this region. The surprising coincidences of band crossing and pressure ionization at certain degrees of compression led McMahan[40] to the conjecture that these phenomena are internally linked and necessarily coincide. The present findings, e.g., those for Li in Sec. III B, show that this is not true in general. We conclude that the coincidence for Al is accidental.

Some details of the energy spectrum of cold-

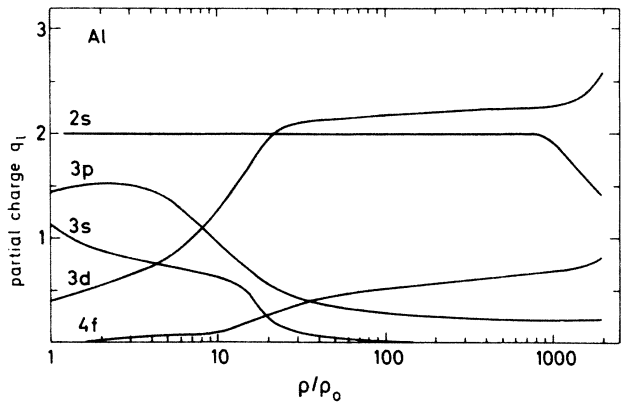

FIG. 14. Partial-wave decomposition of Al valence charge; compare Fig. 5.

TABLE III. Partial charges of Al at different densities.

Partial wave	s	p	d	f	g
Free atom	6	7	0	0	
Normal solid	5.2	7.4	0.4	0	
Compressed solid ($1000\rho_0$)	3.9	6.7	2.3	0.7	
Fermi-gas limit	2.34	4.66	3.82	1.67	0.43

compressed matter are added in Fig. 15 to illustrate the complicated evolution from a normal solid to the asymptotic state comparable with a Fermi gas. The level density $Z(E)$ versus energy E is plotted for various stages of Al compression; the dashed, vertical line marks the Fermi energy. Notice the different scales in Figs. 15(a)–15(d). In Fig. 15(a), the $\sqrt{E}$ distribution characteristic for the free-electron behavior of the valence electrons of Al at normal density is seen; the $2s$ and $2p$ core states are not yet visible. This picture has changed considerably at 6.7-fold compression, shown in Fig. 15(b), where the valence band is now more of p-like character and also the broadened $2s$ and $2p$ core states are seen close to zero energy which is set by the maximum of the electric potential and defines the classical threshold for pressure ionization. Figures 15(c) and 15(d) give the level density for 37- and 100-fold compression, respectively. For $\rho/\rho_0=100$ at a pressure above 10 Gbar, the spectral gap between the L and M shells has closed; however, $Z(E)$ still deviates considerably from the Fermi-gas distribution shown as the dashed line, and one sees regions of lower level density which correspond to particular symmetry points (L,K) of the fcc lattice.

F. Potassium

Finally, we present results for potassium as an example for a heavier alkali metal. The isolated atom has a $4s$ valence electron on top of filled $1s,2s,2p,3s,3p$ core states (compare Fig. 1). Potassium is of particular interest because it shows the isostructural transition due to $s,p\rightarrow d$ reordering even more dramatically than the classical case, cesium (compare Fig. 3); on the other hand, it is much less investigated. Voropinov, Gandelman, and Podvalnyi[12] highlighted the isostructural transition in K which they found from a spherical cell band calculation to occur as a first-order phase transition in the cold-compression curve at a pressure of 180 kbar. Bukowinski[41] presented APW calculations for K below the transition region. More recent theoretical studies on K at high-pressure concentrated on structural phase changes either below the $s\rightarrow d$ transition[42] or above.[43] Here, the emphasis is on the transition region itself.

The cold-pressure versus density, obtained for fcc K, is shown in Fig. 16. One observes a marked flattening at about fivefold compression corresponding to pressures between 500 and 550 kbar. The configuration space used in the ASW calculation contains four core levels ($1s,2s,2p,3s$) and two nonhybridized band configurations ($3p$ and $4s,4p,3d,4f$). The latter is addressed as the valence band. The partial-pressure contributions from the valence and the core ($3p$) electrons are also given in Fig. 16 as dashed lines. It is seen that the valence pressure decreases at high compression and the $3p$-core pressure dominates for $\rho/\rho_0>5$. It was checked that even at the highest calculated pressure the $3s$ state contributed less than 1%.

The $4s,4p\rightarrow 3d$ electron reordering leads to a very pronounced pressure anomaly in potassium. The anomaly is most impressively seen in terms of the bulk modulus in Fig. 3. In order to explain the sharpness of the transition, one needs to have a closer look at what happens at the Fermi surface.

In Fig. 17 the volume dependence of various energy levels at selected symmetry points of the fcc Brillouin zone are plotted relative to the Fermi energy given as horizontal dashed line. What strikes the eye is the crossing of the X_3 and W_2' levels through the Fermi energy

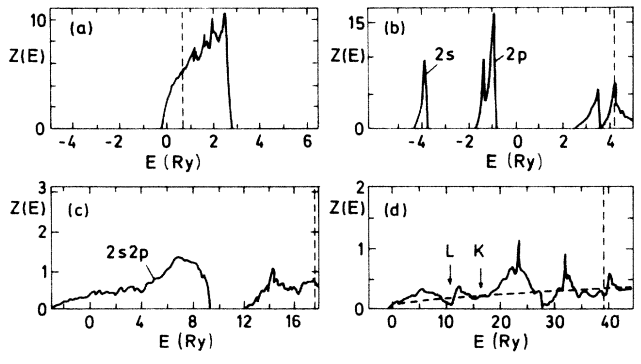

FIG. 15. Energy-level density $Z(E)$ vs energy E for Al at different degrees of compression; (a) normal density, (b) 6.7-fold, (c) 37-fold, and (d) 100-fold compression. The dashed vertical line marks the Fermi energy. In (d) the thick dashed line gives the Fermi-gas distribution for comparison, and the arrows K and L correspond to symmetry points of the fcc Brillouin zone.

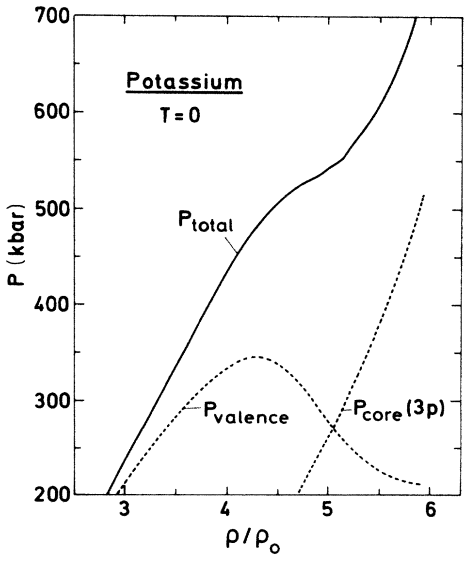

FIG. 16. Cold pressure of potassium vs compression; solid line gives full ASW result; dashed lines give valence and core contributions, respectively.

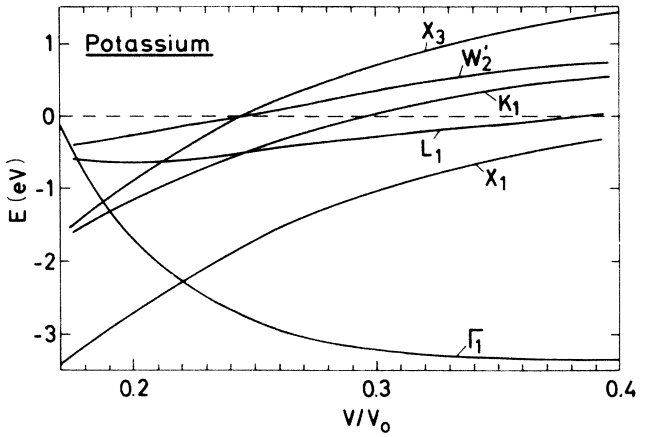

FIG. 17. Electron energies for selected symmetry points (given as curve labels) of the fcc Brillouin zone underlying the K calculation, vs specific volume.

just at the critical volume $v/v_0=0.24$ where the sharp dip in the bulk modulus sets in. As McMahan[40] has pointed out, the states near X_3 have almost pure $3d$ symmetry and their crossing through the Fermi state leads to a much more sudden shift of electrons into the d state than the other redistribution mechanism of s-d hybridization.

A more detailed account of the K results[44] has been published separately. Experimental work on K and also Rb at pressures up to 200 kbar is published in Refs. 45 and 46.

IV. DISCUSSION AND CONCLUSION

The goal of this paper was to study the cold pressure of highly compressed matter in the region 1–1000 Mbar where the transition to statistical-model behavior occurs. The major objective is to learn about the effects of atomic-shell structure on the pressure when compressing materials to extremely high densities. The emphasis is on isostructural changes and pressure ionization. The study is restricted to zero temperature and a fixed lattice structure; structural transitions and the thermal ionic pressure are not included. The study is also restricted to a few light elements—mainly for computational reasons. We hope the selection is sufficient to allow for some general conclusions concerning the systematic trends.

No anomalies due to pressure ionization are found. There is no series of first-order phase transitions due to successive "squeezing of bound states into the continuum" as was conjectured by Kirzhnits. Following the pressure contribution from core states through the region of pressure ionization separately, we do not even find indications for steps or relative softening of the pressure curve. Apparently, the transition from deeply bound, discrete electron states to completely free electrons proceeds through many stages of gradual state broadening and resonance formation of nearly bound electrons, thus completely smoothing any sudden effect on the pressure. As More[10] has put it, pressure ionization is continuous. For the first time, the present paper provides explicit and systematic evidence for this.

Let us briefly comment on results reported in the literature which seem to support the opposite standpoint. They can be readily attributed to alternative mechanisms as shown in this paper. Wiggles in the cold-pressure curve of Al, found by McMahan and Ross[13] and interpreted as evidence for L- and K-shell pressure ionization, appear to originate from $3sp\rightarrow 3d$ and $2s\rightarrow 3d$ band crossings which happen to occur in Al at same compression as L- and K-shell pressure ionization, respectively. Deviations between band-structure and statistical-model calculations for cold Li in the 100-Mbar region, reported by Ross[7] and attributed to pressure ionization of the $1s$-core state, are not confirmed in the present Li calculations. This may result from the difference between the quantum-statistical model, which includes gradient corrections and is used here, and the Thomas-Fermi-Dirac approximation chosen by Ross; QSM is superior. Indications for shell structure have also been reported for shock adiabatics at very high pressures, both theoretically[1,8] and experimentally.[3] However, one should notice that the generation of dynamic pressures in the region of 100 Mbar and above is connected with considerable heating of the shocked material (order of 100 eV). Shell effects are expected in this context due to thermal ionization which should be clearly distinguished from the pressure ionization investigated here.

The second important finding concerns isostructural transitions. A very clear and comprehensive discussion of this subject was given by McMahan.[40] It is the mechanism of band crossing and corresponding reordering of valence electrons which leads systematically to oscillations of the cold-pressure curve relative to the smooth QSM prediction. More's results[14] for Al, comparing high-quality APW calculations of McMahan with QSM, showed that these oscillations persist to very high pressures with deviations from QSM of order 5% at 1 Gbar and 0.5% at 100 Gbar. The present paper extends these results to other elements and emphasizes their interpretation. We find deviations between QSM and the present ASW calculations of typically 10–20% for He, Li, Be, and Al in the region 10–100 Mbar. For metals, the pressure in this region is almost exclusively generated by the valence electrons.

For interpreting the pressure oscillations, one has to notice that valence electrons in different partial waves react differently upon compression. This is because they have different spatial extension. Typically, waves of low angular momentum, particularly s waves, are energetically favored in isolated atoms and solids of normal density, but under compression their energy is shifted upwards relative to waves of higher angular momentum which are more easily accommodated in the decreasing cell space available. The corresponding redistribution of electrons leads to pressure relaxation, and due to the stepped nature of the energy spectrum oscillations occur. The change from lower to higher angular momentum is taken as the general guideline in our presentation. Ultimately, at extreme compression, the limit of a free and uniform Fermi gas enclosed in a small spherical volume should be approached; the corresponding angular-momentum

decomposition was calculated and used for comparison.

Strong pressure anomalies due to the mechanism just described are found in alkali metals because they have a single valence electron of predominantly s-wave character. It is the $6s \rightarrow 5d$ reordering which causes the well-known isostructural phase transition in Cs observed at 44 kbar.[47] In the present paper we find related anomalies in Li at about 10 Mbar due to $2s \rightarrow 2p$ reordering and in K at 500 kbar due to $4s,4p \rightarrow 3d$ reordering. It is seen that the critical pressure strongly decreases with atomic number; it roughly scales like $Z^{-1/2}$. In the cold-pressure curves, the anomalies show up as shoulders rather than real pockets. The same was found by Glötzel and McMahan[48] for Cs at $T=0$, and the first-order phase transition actually observed in Cs at room temperature was attributed to a phonon anomaly, which, in turn, was directly related to the $T=0$ results. We consider it unlikely that corresponding first-order phase transitions will occur in K and Li because of the much higher pressures involved; nevertheless, the present results strongly suggest an experimental investigation of these two materials.

ACKNOWLEDGMENTS

The authors thank Professor J. Kübler for making his augmented-spherical-wave code available to them, for his continuous advice on how to use it, and for many very helpful discussions on the topic of this paper. This work was supported in part by the Bundesministerium für Forschung und Technologie (Bonn, Germany) and by EURATOM.

APPENDIX A: SOLVING QSM

Solving the QSM equations (17)–(19) is a nontrivial numerical problem. Several methods[14,28,49] have been described in the literature. In the present work, we used the transformation

$$n(r)=\exp[y(r/a_B)]/a_B^3 \ . \tag{A1}$$

Measuring all lengths in a_B and all energies in Ry, one obtains

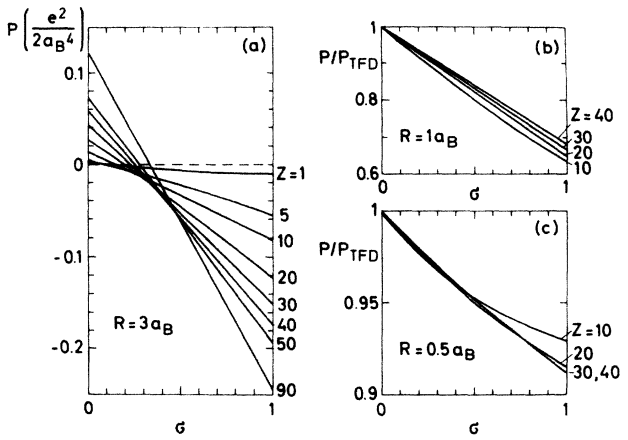

FIG. 18. Dependence of QSM pressures on the strength σ of the gradient term. The different curves correspond to materials with different Z, which is given as the label. (a)–(c) give results for different Wigner-Seitz radii R.

TABLE IV. Thomas-Fermi-Dirac pressure in $(e^2/2a_B^4)$.

$R=1a_B$		$R=0.5a_B$	
Z	P_{TFD}	Z	P_{TFD}
10	5.12	10	301
20	13.1	20	850
30	22.1	30	1540
40	31.6	40	2320

$$y''(x)=-[y'(x)]^2/2-(2/x)[y'(x)+2Z/\sigma] +(2/\sigma)[V-E_F+(3\pi^2 e^y)^{2/3}] \ , \tag{A2}$$

with boundary conditions $y'(0)=-2Z/\sigma$ and $y'(R_0/a_B)=0$. The potential V in Eq. (A2) is assumed to contain the electron and exchange-correlation contributions; the nuclear potential is represented explicitly by the singular term $(2/x)(2Z/\sigma)$, which is compensated by the term $(2/x)y'(x)$ at $x=0$ so that no singularity occurs at the origin. However, with increasing Z and decreasing σ the solution $y(x)$ becomes rather steep in the center and is difficult to obtain numerically. The code BOUNDS based on the multiple shooting method[50] is used to solve Eq. (A2) for an approximate V which is then recalculated with the new density (A1). This process is iterated until convergence is reached.

Results on the σ dependence on the QSM pressure are shown in Fig. 18. In Fig. 18(a), the pressure is given for a Wigner-Seitz radius $R_0=3a_B$, which corresponds rough-

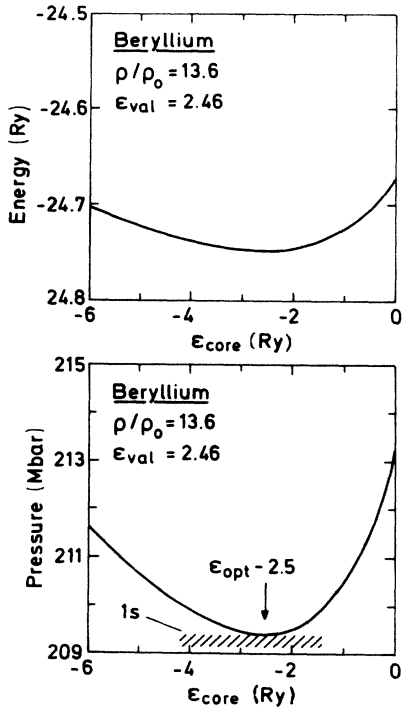

FIG. 19. Total energy (upper) and pressure (lower) of Be at 13.6-fold compression as a function of the constant interstitial potential V_{core} chosen for the $1s$ core band; the corresponding value for the valence band V_{val} is kept fixed at its optimal value 2.46 Ry; the width of the $1s$ core band is given as shaded region.

ly to matter at normal density. The different lines refer to materials with different Z, which is given as a label on the right-hand side. The pressure is given in atomic units ($e^2/2a_B^4$). Note that from $Z=30$ to 90 the σ dependence is almost linear and allows for simple interpolation as soon as the pressures for $\sigma=0$ (Thomas-Fermi-Dirac model) and $\sigma=1$ (QSM with Weizsäcker's value) are known. How the σ dependence evolves under compression is shown in Figs. 18(b) and 18(c). For reasons of comparison the pressures are normalized to their values at $\sigma=0(p_{\rm TFD})$, given in Table IV. The σ dependence for the normalized pressure shown in Fig. 18(b) at $R_0=1a_B$ is roughly linear and similar for all investigated Z. It is strongest for small Z and smallest for high Z. Compressing further to $R=0.5a_B$, as shown in Fig. 18(c), the branch for small Z values is bent upwards (note the enlarged scale), indicating that low-Z materials reach their high-density Thomas-Fermi-Dirac limit at lower density than high-Z materials.

APPENDIX B: CHOICE OF INTERSTITIAL ENERGY ε FOR ASW

In linearized muffin-tin band-structure calculations such as the ASW method, the energy parameter $\varepsilon=E-V_0$ in the interstitial region between the spherical cells is usually chosen to be constant.[51] Having in mind the variational character of the ASW method, we have taken ε as a variational parameter. In the present ASW calculations, the optimization was generally performed for each material at each compression point. In cases with several bands (e.g., when discrete core levels split) we optimized ε for each band separately. As a result of the ε variation, pressure lowering of typically a few percent, relative to the pressure obtained for $\varepsilon=0$, was found; in extreme cases, such as K at 700 kbar, it amounted to 10%.

The ε variation is illustrated in Fig. 19 for the 1s core band of Be at 13.6-fold compression. Optimization of the valence band led to $\varepsilon_{\rm val}=2.46$. The variation of the total energy (upper part) and the corresponding pressure (lower part) is shown as a function of $\varepsilon_{\rm core}$, which is the ε of the 1s core band; this band is shown as a shaded region extending from -4.2 to -1.4 Ry. The optimum of the variation is located at $\varepsilon_{\rm core}=-2.5$ Ry, which coincides with the calculated band center

$$\int Z_{1s}(E)E\,dE \Big/ \int Z_{1s}(E)dE = -2.5 \text{ Ry} .$$

*Present address: Fraunhofer-Institut für Festkörpertechnologie, Paul-Gerhardt-Allee 42, 8000 München 60, Federal Republic of Germany.

[1]S. I. Anisimov, A. M. Prochorov, and V. E. Fortov, Usp. Fiz. Nauk **142**, 395 (1984) [Sov. Phys.—Usp. **27**, 181 (1984)]; R. M. More, in *Laser Interaction and Related Plamsa Phenomena,* edited by H. J. Schwarz, H. Hora, M. J. Lubin, and B. Yaakobi (Plenum, New York, 1981), Vol. 5, p. 253.

[2]R. Arnold and J. Meyer-ter-Vehn, Rep. Prog. Phys. **50** (1987).

[3]C. E. Ragan III, Phys. Rev. A **29**, 1391 (1984); A. S. Vladimirov, N. P. Voloshin, V. N. Nogin, A. V. Petrovtsev, and V. A. Simonenko, Pis'ma Zh. Eksp. Teor. Fiz. **39**, 69 (1984) [JETP Lett. **39**, 82 (1984)].

[4]J. Nuckolls, L. Wood, A. Thiessen, and G. Zimmermann, Nature (London) **239**, 139 (1972).

[5]A. V. Bushman and V. E. Fortov, Usp. Fiz. Nauk **140**, 177 (1983) [Sov. Phys.—Usp. **26**, 465 (1983)].

[6]B. K. Godwal, S. K. Sikka, and R. Chidambaram, Phys. Rep. **102**, 121 (1983).

[7]M. Ross, Rep. Prog. Phys. **48**, 1 (1985).

[8]D. A. Kirzhnits and G. V. Shpatakovskaya, Zh. Eksp. Teor. Fiz. **66**, 1828 (1974) [Sov. Phys.—JETP **39**, 899 (1975)]; D. A. Kirzhnits, Yu. E. Lozovik, and G. V. Shpatakovskaya, Usp. Fiz. Nauk **117**, 3 (1975) [Sov. Phys.—Usp. **18**, 649 (1976)].

[9]J. W. Zink, Phys. Rev. **176**, 279 (1968).

[10]R. M. More, in *Advances in Atomic and Molecular Physics,* edited by D. R. Bates and I. Estermann (Academic, New York, 1985), Vol. 21, p. 305.

[11]C. M. Lee and E. I. Thorsos, Phys. Rev. A **17**, 2073 (1978).

[12]A. I. Voropinov, G. M. Gandelman, and V. G. Podvalnyi, Usp. Fiz. Nauk **100**, 193 (1970) [Sov. Phys.—Usp. **13**, 56 (1970)].

[13]A. K. McMahan and M. Ross, in *High Pressure Science and Technology,* edited by K. D. Timmerhaus and M. S. Barber (Plenum, New York, 1979), Vol. 2, p. 920.

[14]R. M. More, Phys. Rev. A **19**, 1234 (1979).

[15]A. R. Williams, J. Kübler, and C. D. Gelatt, Jr., Phys. Rev. B **19**, 6094 (1979).

[16]N. W. Ashcroft and N. D. Mermin, *Solid State Physics* (Saunders College, Philadelphia, 1981).

[17]W. Zittel, Ph.D. thesis, Technische Hochschule Darmstadt, 1986 (unpublished); and Max-Planck-Institut für Quantenoptik, Report No. MPQ 111, 1986 (unpublished).

[18]P. Hohenberg and W. Kohn, Phys. Rev. **136**, B864 (1964).

[19]C. F. von Weizsäcker, Z. Phys. **96**, 431 (1935).

[20]A. S. Kompaneets and E. S. Pavlovskii, Zh. Eksp. Teor. Fiz. **31**, 427 (1956) [Sov. Phys.—JETP **4**, 328 (1957)]; D. A. Kirzhnits, *ibid.* **32**, 115 (1957) [**5**, 64 (1957)].

[21]W. Jones and W. H. Young, J. Phys. C **4**, 1322 (1971).

[22]J. C. Slater, in *Advances in Quantum Chemistry* (Academic, New York, 1972), Vol. 6, p. 1.

[23]U. von Barth and L. Hedin, J. Phys. C **5**, 1629 (1972).

[24]L. H. Thomas, Proc. Cambridge Philos. Soc. **32**, 542 (1927); E. Fermi, Z. Phys. **48**, 73 (1928).

[25]R. P. Feynman, N. Metropolis, and E. Teller, Phys. Rev. **75**, 1561 (1949); R. D. Cowan and J. Ashkin, *ibid.* **105**, 144 (1957).

[26]D. A. Kirzhnits, Zh. Eksp. Teor. Fiz. **35**, 1545 (1958) [Sov. Phys.—JETP **8**, 1081 (1959)]; N. N. Kalitkin, *ibid.* **38**, 1534 (1960) [**11**, 1106 (1960)]; S. L. McCarthy, UCRL (University of California Radiation Laboratory) Report No. 14364, 1965 (unpublished).

[27]N. N. Kalitkin and L. V. Kuz'mina, Fiz. Tverd. Tela (Leningrad) **13**, 2314 (1971) [Sov. Phys.—Solid State **13**, 1938 (1972)].

[28]F. Perrot, Physica A **98**, 555 (1979); F. Perrot, Phys. Rev. A

20, 586 (1979).
[29]O. K. Andersn, Phys. Rev. B **12**, 3060 (1975).
[30]W. Zittel, J. Meyer-ter-Vehn and J. Kübler, Physica B + C **139&140B**, 364 (1986); W. Zittel, J. Meyer-ter-Vehn, J. C. Boettger, and S. B. Trickey, J. Phys. F **15**, L247 (1985).
[31]J. C. Boettger and S. B. Trickey, Phys. Rev. B **32**, 3391 (1985).
[32]D. A. Liberman, Colloques Internationaux du Centre de la Recherche Scientifique No. 188, Grenoble, 1969, pp. 35–41 (unpublished).
[33]The hcp structure for He is quoted in Ref. 16.
[34]D. A. Young, A. K. McMahan, and M. Ross, Phys. Rev. B **24**, 5119 (1981).
[35]N. H. March, in *Advances in High Pressure Research*, edited by R. S. Bradley (Academic, London, 1969), Vol. 3, p. 241.
[36]F. Perrot, Phys. Rev. B **21**, 3167 (1980).
[37]M. Y. Chou, P. K. Lam, and M. L. Cohen, Phys. Rev. B **28**, 4179 (1983).
[38]N. M. Amonenko, V. Ye. Ivanov, G. F. Tikhinskij, and V. F. Finkel, Fiz. Met. Metalloved. **14**, 852 (1962) [Phys. Met. Metallogr. USSR **14**, 47 (1962)].
[39]P. K. Lam and M. L. Cohen, Phys. Rev. B **27**, 5986 (1983).
[40]A. K. McMahan, Physica B + C **139&140B**, 31 (1986).
[41]M. S. T. Bukowinski, in *High Pressure Science and Technology*, edited by K. D. Timmerhaus and M. S. Barber (Plenum, New York, 1979), Vol. 2, p. 237.
[42]H. L. Skriver, Phys. Rev. B **31**, 1909 (1985).
[43]A. K. McMahan, Phys. Rev. B **29**, 5982 (1984).
[44]W. Zittel, J. Meyer-ter-Vehn, and J. Kübler, Solid State Commun. **62**, 97 (1987).
[45]K. Takemura and K. Syassen, Solid State Commun. **44**, 1161 (1982).
[46]H. Olijnyk and W. B. Holzapfel, Phys. Lett. **99A**, 381 (1983).
[47]P. W. Bridgman, Proc. Am. Acad. Arts Sci. **76**, 55 (1948); R. Sternheimer, Phys. Rev. **78**, 235 (1950).
[48]D. Glötzel and A. K. McMahan, Phys. Rev. B **20**, 3210 (1979).
[49]W. Stich, E. K. U. Gross, P. Malzacher, and R. M. Dreizler, Z. Phys. A **309**, 5 (1982).
[50]J. Stoer and R. Bulirsch, *Einführung in die numerische Mathematik* (Springer, Berlin, 1978), Vol. 2.
[51]O. Gunnarsson, J. Harris, and R. O. Jones, J. Phys. C **9**, 2739 (1976).